PNAS RESEARCH ARTICLE | BIOPHYSICS AND COMPUTATIONAL BIOLOGY

Structural insights into a spindle-shaped archaeal virus with a sevenfold symmetrical tail

Zhen Han[a,1], Wanjuan Yuan[b,c,1], Hao Xiao[a], Li Wang[b], Junxia Zhang[b], Yuning Peng[a], Lingpeng Cheng[a,d,2], Hongrong Liu[a,2], and Li Huang[b,c,2]

Edited by Stephen Goff, Columbia University Irving Medical Center, New York, NY; received October 25, 2021; accepted May 4, 2022

Archaeal viruses with a spindle-shaped virion are abundant and widespread in extremely diverse environments. However, efforts to obtain the high-resolution structure of a spindle-shaped virus have been unsuccessful. Here, we present the structure of SSV19, a spindle-shaped virus infecting the hyperthermophilic archaeon *Sulfolobus* sp. E11-6. Our near-atomic structure reveals an unusual sevenfold symmetrical virus tail consisting of the tailspike, nozzle, and adaptor proteins. The spindle-shaped capsid shell is formed by seven left-handed helical strands, constructed of the hydrophobic major capsid protein, emanating from the highly glycosylated tail assembly. Sliding between adjacent strands is responsible for the variation of a virion in size. Ultrathin sections of the SSV19-infected cells show that SSV19 virions adsorb to the host cell membrane through the tail after penetrating the S-layer. The tailspike harbors a putative endo-mannanase domain, which shares structural similarity to a *Bacteroides thetaiotaomicro* endo-mannanase. Molecules of glycerol dibiphytanyl glycerol tetraether lipid were observed in hydrophobic clefts between the tail and the capsid shell. The nozzle protein resembles the stem and clip domains of the portals of herpesviruses and bacteriophages, implying an evolutionary relationship among the archaeal, bacterial, and eukaryotic viruses.

archaeal virus | cryo-EM structure | sevenfold symmetrical tail

Significance

Spindle-shaped viruses are among the most prominent archaeal viruses and widespread in diverse habitats. Here, we present the structure of a spindle-shaped virus (SSV19) that infects a hyperthermophilic archaeon. Our results show that SSV19 is formed by seven left-handed helical strands starting from an unusual sevenfold symmetrical tail, with which the virus adsorbs to the host cell. The tailspike harbors a putative endo-mannanase domain, which presumably binds or degrades mannose-containing glycan chains on the cell membrane. The tail nozzle protein resembles the stem and clip domains of the portals of herpesviruses and bacteriophages. These findings shed significant light on the morphogenesis of and host entry by spindle-shaped viruses and imply an evolutionary relationship among the archaeal, bacterial, and eukaryotic viruses.

Viruses infect hosts in all three domains of life (1–3). Archaeal viruses are far more diverse in shape and less well-studied than Bacteria and Eukarya viruses are (4, 5). Among the morphologically unique archaeal viruses, spindle-shaped viruses are found in archaea inhabiting acidic hot springs, hypersaline, and marine environments (6). *Sulfolobus* spindle-shaped viruses (SSVs) of the family *Fuselloviridae*, which infect hyperthermophilic archaea of *Sulfolobales* in hot springs, are among the most widespread and best characterized archaeal viruses (7). Fuselloviruses are divided into two genera (i.e., *Alphafusellovirus* and *Betafusellovirus*), which are similar in capsid shell but differ distinctly in tail structure (8). An SSV virion consists of a spindle-shaped capsid shell that encapsidates a circular double-stranded DNA (dsDNA) genome and has a tail at one end for host attachment (9). Efforts have been made to elucidate the structural basis of the morphogenesis, stability, and host recognition and adsorption of fuselloviruses (8, 10, 11). A cryo-electron microscopy (cryo-EM) reconstruction at ∼32 Å resolution indicated that *Sulfolobus* spindle-shaped virus 1 (SSV1) has a sixfold symmetrical tail structure (12). A cryo-electron tomography (cryo-ET) reconstruction at ∼20 Å resolution revealed that His1, which morphologically resembles SSVs and infects the extremely halophilic euryarchaeon *Haloarcula hispanica*, has a variable capsid structure and a uniform tail hub surrounded by six tailspikes (13). However, the lack of high-resolution structures of complete capsids prevents an in-depth structural understanding of this unique morphotype of archaeal viruses.

Fuselloviruses are known to contain four structural proteins, i.e., the major capsid protein (MCP) VP1, the DNA binding protein VP2, the minor capsid protein VP3 and the tail filament protein VP4 (8). However, the structures and organizational roles of these proteins remain to be elucidated. Here, we report the structure of SSV19, a recent addition to the family *Fuselloviridae*, genus *Betafusellovirus* (8). We show that the SSV19 virion has a spindle-shaped capsid formed by seven left-handed helical strands emanating from a sevenfold symmetrical tail assembly. The structure of the tail permits the identification of sites of extensive glycosylation in tail proteins, an endo-mannanase-homologous domain in the tailspike, and lipid molecules in clefts surrounding the tail. Ultrathin sections of the SSV19-infected cells show that SSV19 adopts mechanisms of cell adsorption and genome delivery similar to those of short-tailed bacteriophages. The results shed significant light on the mechanisms of host recognition and genome delivery by the spindle-shaped viruses, and suggests an evolutionary relationship among the archaeal SSVs, herpesviruses, and bacteriophages.

Author contributions: L.C., H.L., and L.H. designed research; Z.H., W.Y., H.X., L.W., J.Z., Y.P., L.C., H.L., and L.H. performed research; H.L. and L.H. contributed new reagents/analytic tools; Z.H., W.Y., H.X., L.W., J.Z., Y.P., L.C., H.L., and L.H. analyzed data; and Z.H., W.Y., L.C., H.L., and L.H. wrote the paper.

The authors declare no competing interest.

This article is a PNAS Direct Submission.

[1]Z.H. and W.Y. contributed equally to this work.

[2]To whom correspondence may be addressed. Email: huangl@im.ac.cn or hrliu@hunnu.edu.cn or lingpengcheng@hunnu.edu.cn.

This article contains supporting information online at http://www.pnas.org/lookup/suppl/doi:10.1073/pnas.2119439119/-/DCSupplemental.

Published July 27, 2022.

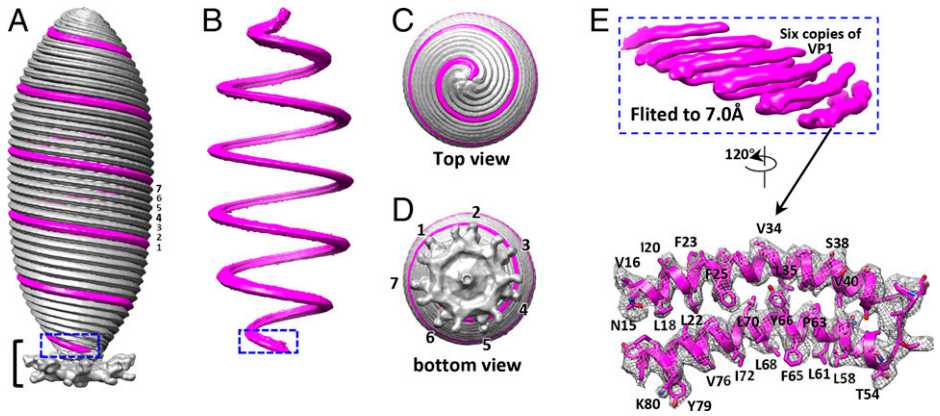

Fig. 1. Structure of SSV19. (*A*) Cryo-EM structure of SSV19 at 10 Å resolution. One of the seven strands is colored in magenta. (*B*) A strand from the capsid in (*A*) (magenta). (*C*) and (*D*) Top and bottom views of the SSV19 capsid. (*E*) A 7-Å resolution structure of MCP VP1 subunits in the segment of a strand shown in blue dashed box in (*A*) and (*B*), and an atomic model of a VP1 subunit superimposed on its density map (mesh).

Overall Structure of SSV19. *Sulfolobus* sp. E11-6 containing SSV19 was grown to the stationary phase, and virus particles were harvested and purified by two runs of cesium chloride density gradient centrifugation. Approximately 109,800 virus particles from 3,770 micrographs, collected under a 200 kV FEI Arctica electron microscope, were selected for three-dimensional (3D) reconstruction (*SI Appendix*, Fig. S1*A*). The particles were classified by capsid shape into four subsets by using Relion software (14). All the capsid structures comprise a helical spindle-shaped body and a sevenfold symmetrical tail assembly (*SI Appendix*, Fig. S1*B*). This symmetry has never been observed in other virus tails. The resolutions of the four types of capsid structures were improved to ∼10 Å by applying sevenfold symmetry (*SI Appendix*, Fig. S1*C*). The virus capsid is formed by seven left-handed helical strands emanating from the sevenfold symmetrical tail assembly (Fig. 1*A*–*D*). The distance between adjacent strands along the long axis is 22 Å in each of these capsids (*SI Appendix*, Fig. S1*C*). Although the four types of capsids differ in size, their tail assemblies are identical (*SI Appendix*, Fig. S1 *B* and *C*). A four-layered structure exists within the capsid shell. The distance between the two adjacent layers is ∼27 Å (*SI Appendix*, Fig. S1*D*). The layered structure is presumably formed by the SSV19 DNA in complex with proteins.

Tail Structure. Further local reconstructions increased the resolution of the tail assembly and the adjacent portion of the capsid to 3.8 Å (*SI Appendix*, Fig. S2). The tail consists of a nozzle, an adaptor, and tailspikes, resembling the tails of short-tailed bacteriophages (15, 16). We identified and built atomic models for the major capsid protein (MCP) VP1 and for the tail assembly formed by nozzle protein C131, adaptor protein B210, and tailspike protein VP4 (Fig. 2) based on main chains and bulky side chains in the density map (*SI Appendix*, Fig. S2).

The resolved C131 structure (residues 2–125) is a four-helix bundle (Fig. 3*A*). Seven C131 subunits form a heptameric funnel-like tail nozzle with a channel at the center (Fig. 3*A* and *B*). The top and bottom ends of the channel are 20 and 12 Å in diameter, respectively (Fig. 3*B*). The main body of the nozzle is formed by the four-helix bundle of the protein, whereas the tip is formed by a β-hairpin (residues 45–60) between helices α2 and α3. The architecture of the C131 is similar to the stem and clip (β-tunnel) domains of bacteriophages (16–19) and herpesviruses (20, 21) (Fig. 4). A plug-like structure, which is located at the N- and C-terminal regions of the seven C131 subunits and blocks the nozzle channel, is probably formed by the unresolved N- and C-terminal residues of the protein (*SI Appendix*, Fig. S3).

The nozzle is surrounded by seven copies of tailspike protein VP4 (Figs. 2*A* and *B* and 3*C* and *SI Appendix*, Fig. S4). Of 1,236 residues in VP4, 456 were modeled (*SI Appendix*, Figs. S2*C* and S5). The resolved parts of VP4 comprise three domains (Fig. 3*D*), a pseudo sixfold core (residues 27–115, 588–677, 902–936, and 973–1048), a β-sandwich (residues 1049–1142), and a Z-shaped three-helical bundle (residues

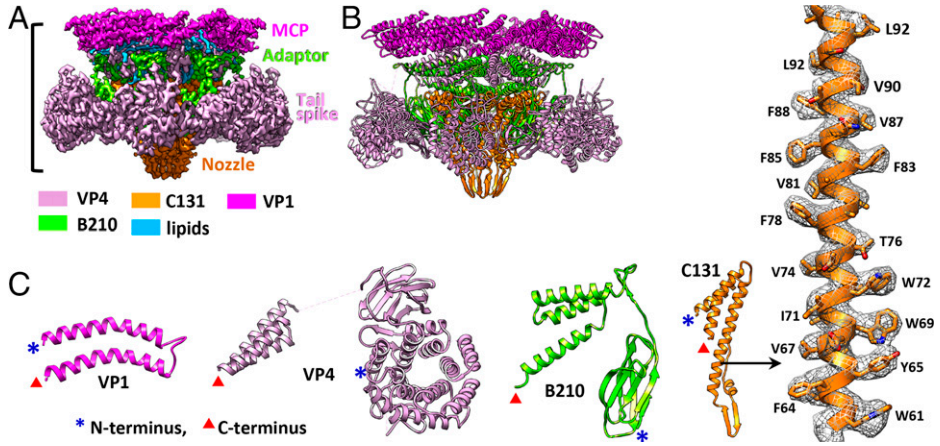

Fig. 2. Structure of the SSV19 tail. (*A*) Density map of the sevenfold symmetrical tail and adjacent MCP VP1 subunits at 3.8 Å. (*B*) Atomic models of the tail and VP1 subunits. (*C*) Atomic models of the tail proteins and MCP VP1.

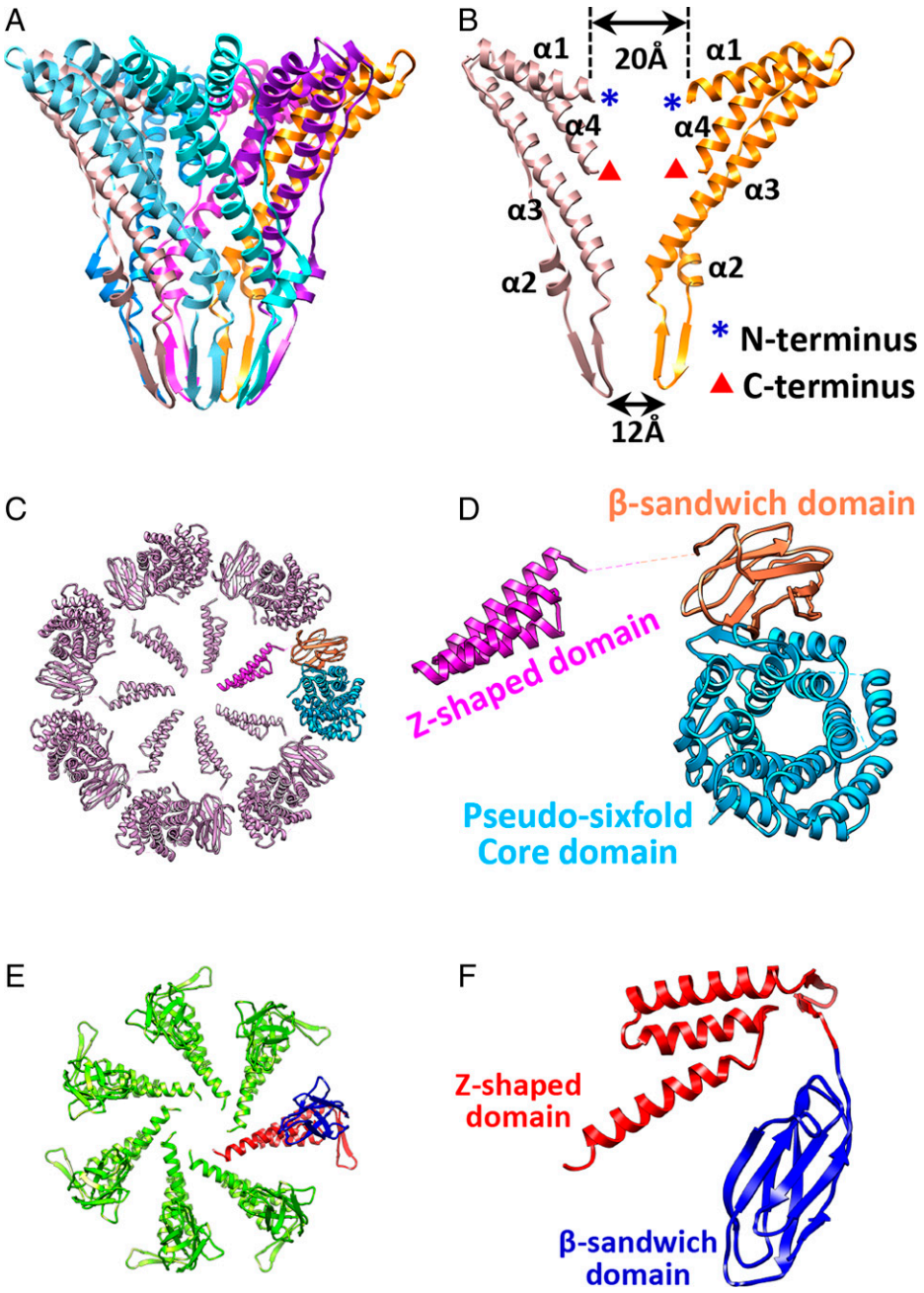

Fig. 3. Structures of the tail proteins. (*A*) Heptamer of tail nozzle protein C131 (*Side* view). Seven C131 subunits are in different colors. (*B*) Slab view of the nozzle. Only two subunits are shown. The resolved N and C termini are marked. (*C*) Heptamer of tailspike protein VP4 (*Bottom* view). One of the seven subunits is colored by domains. (*D*) Zoom-in view of the VP4 subunit. (*E*) Heptamer of tail adaptor protein B210 (*Bottom* view). One of the seven subunits is colored by domains. (*F*) Zoom-in view of the B210 subunit.

1162–1233). Two protrusions from each tailspike protein are resolved only at lower resolution (*SI Appendix*, Fig. S4) presumably due to their flexibility. These protrusions are formed by the unmodeled residues 116–587, 678–901, and 937–972, which are inserted segments in the core. These unresolved residues appear to form mostly β-sheets according to the density map at 7-Å resolution, in agreement with the VP4 secondary structure (*SI Appendix*, Figs. S4 and S5) predicted with PSIPRED (22). The flexibility of these β-sheets is consistent with the role of the tailspikes in receptor recognition and adsorption during viral infection (23). Unresolved residues 1143–1161 leave a gap between the Z-shaped three-helical bundle and the other two domains in the VP4 density map (Fig. 3*D*).

The adaptor protein B210 also contains a β-sandwich and a Z-shaped three-helical bundle domain connected by a β-hairpin structure (Fig. 3*E* and *F*). Seven copies of three-helical bundles in B210 and seven in VP4 form a ring, which mediates the assembly of the nozzle onto the capsid. Seven copies of the B210 β-sandwich attach to the surface of the nozzle and interact with its side, allowing the VP4 cores and β-sandwiches to attach to the nozzle (*SI Appendix*, Movie S1).

A number of glycosylation sites were identified on the structures of tail proteins VP4 and B210 (*SI Appendix*, Fig. S6). All these sites contain the conserved motif NXT (where X represents any amino acid other than proline), indicating that the sites are N-glycosylated. The majority of these glycosylated sites are located at the turns and oriented outward (*SI Appendix*, Fig. S6),

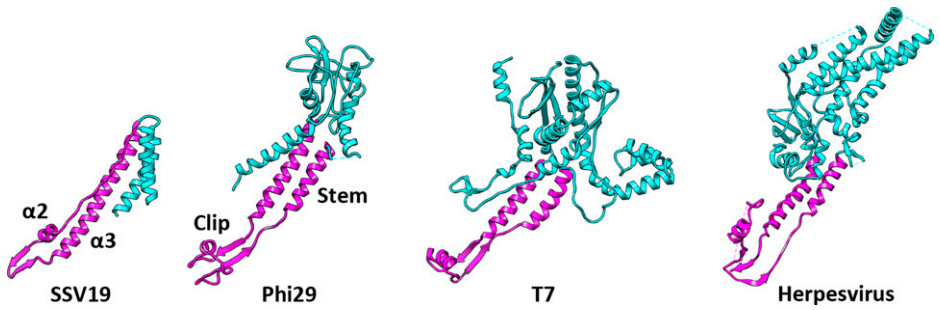

Fig. 4. Structural comparison of SSV19 C131, portal proteins of phage Phi29, phage T7, and herpesvirus (Epstein-Barr virus). The stem and clip domains are in magenta.

suggesting that they may play roles in protein folding, stabilization, and host receptor recognition.

VP4 Core. Intriguingly, a search of the Protein Data Bank using the Dali server shows that the VP4 core domain resembles an endo-mannanase from glycoside hydrolase family 76 (GH76) from a *Bacteroides thetaiotaomicro* strain (24). The GH76 enzymes, which are present in bacteria and fungi, cleave debranched linear α-1,6-mannan. The VP4 core is topologically similar to the catalytic domain of the endo-mannanase, comprising a classic α/α6 core of a pseudo sixfold helical barrel. If the endo-mannanase is rotated 60° around the pseudo sixfold axis, then two consecutive aspartate residues (Asp69 and Asp70) in the VP4 core would overlap nicely with the putative catalytic nucleophile Asp258 and acid/base Asp259 in the endo-mannanase (Fig. 5 and *SI Appendix*, Fig. S7). The mutation of the two aspartate residues to asparagine (Asp258Asn and Asp259Asn) was demonstrated to ablate the catalytic activity of the endo-mannanase (24). In addition, residues (Trp196, Phe256, and Tyr386) around the active site in the endo-mannanase, which interact with substrate, are similarly positioned in VP4 (Trp1033, Phe66, and Tyr640) (Fig. 5 and *SI Appendix*, Fig. S7). Sequence alignments of SSV19 VP4 and its homologous proteins, including those from other betafuselloviruses, show that these key residues are conserved (*SI Appendix*, Fig. S8). *Sulfolobus* species are known to possess an extensively N-glycosylated S-layer, and mannose is often part of the glycan chains (25, 26). SSV19 VP4 would presumably bind to and possibly degrade the glycan chain, facilitating host recognition and genome delivery by the virus.

MCP VP1. Residues 15–83 of the 84-residue VP1 at the tail-proximal end of the capsid shell were modeled (Fig. 1*E* and *SI Appendix*, Fig. S9*A*). VP1 consists of two curved α-helices (residues 15–44 and 54–83) connected by a loop (residues 45–53). The VP1 protein folds as a curved hydrophobic α-hairpin, as

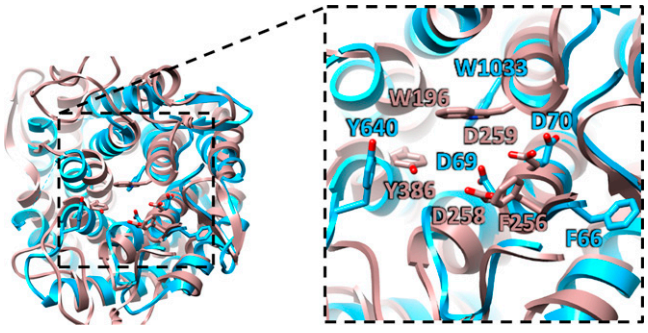

Fig. 5. Structural comparison of the VP4 core (cyan) and the catalytic domain (brown) of *Bacteroides thetaiotaomicro* endo-mannanase.

shown for the MCP of the rod-shaped archaeal virus APBV1 (27). Each VP1 subunit in the bottom layer stacks on the Z-shaped three-helical bundle of VP4 through hydrophobic interactions, forming the starting point for one of the seven left-handed helical strands that make up the spindle-shaped capsid (*SI Appendix*, Fig. S9 *B–D*). The neighboring VP1 subunits within a strand or between two adjacent strands interact through strong hydrophobic interactions between their α-helices (*SI Appendix*, Fig. S9*C*), as is observed in the capsids of other viruses infecting hyperthermophilic archaea (27), presumably contributing to virus stability at high temperature. The N terminus of the α-helix 1 and the C terminus of the α-helix 2 from each VP1 subunit form the inner surface, whereas the loop between the two α-helices makes up the outer surface of the capsid shell. Both the N and C termini of VP1 are not well resolved presumably due to their flexibility. The N-terminal region, which is rich in arginine residues (*SI Appendix*, Fig. S9*E*), probably interacts with the viral genomic DNA. The architecture of the SSV19 capsid is consistent with the suggestion that all spindle-shaped viruses form capsids through multistart helical assembly, as was inferred from the crystallographic structure of the recombinant MCP of the spindle-shaped archaeal virus ATSV (28). Both intra- and interstrand interactions exist between VP1 subunits via helices in the capsid. The distance between interacting helices from two adjacent VP1 subunits in the same strand appears shorter than that between VP1 subunits of the two adjacent strands, suggesting a stronger interaction between VP1 subunits within the strand than that between the strands. Variation in capsid size may therefore be achieved by subtle sliding of a strand in relation to the adjacent one. Except for the region next to the tail, the capsid shell was not resolved at near-atomic resolution, suggesting that the capsid shell was highly malleable in shape.

Virus Lipids. It was shown that SSV1 contained host-derived glycerol dibiphytanyl glycerol tetraether (GDGT) lipids with various headgroups (29). However, the location of the lipids in a fusellovirus virion is unclear although they were suggested to exist in an envelope encasing the viral capsid (30). As shown by thin-layer chromatography, SSV19 contains lipids similar to those of the host cell membrane (*SI Appendix*, Fig. S10*A*). However, no lipid layer was observed on the surface of the SSV19 virion. Intriguingly, loop-like structures were found in the clefts between the capsid and tail (Figs. 2*A* and 6*A* and *SI Appendix*, Fig. S11). Their exclusive interaction with the hydrophobic residues of the tail proteins and lack of side chains raises the possibility that these structures are GDGT lipids. This hypothesis is supported by the fact that a model of a GDGT-5 lipid (or models of other GDGT lipids) with two inositol phosphate headgroups (31) fits well with the density of the closed loop (Fig. 6*B*). These lipids are likely acquired in the host

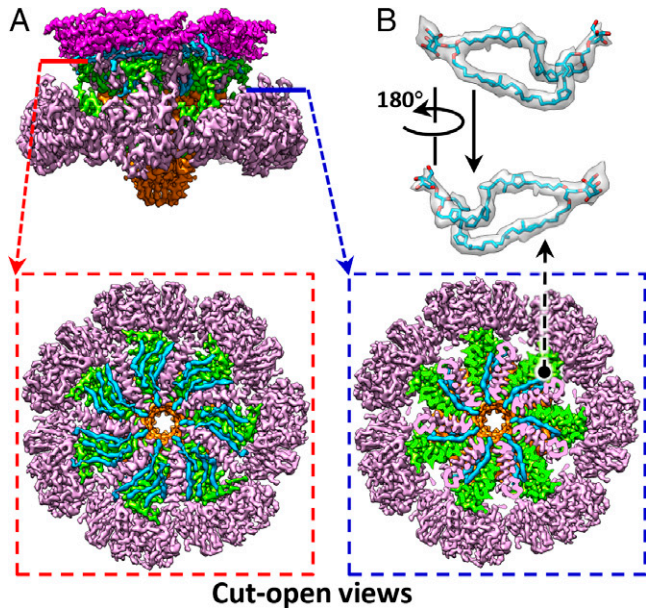

Fig. 6. GDGT lipids in the capsid. (*A*) GDGT lipids in two clefts between the capsid shell and tail. (*B*) A typical GDGT molecule (GDGT-5 is modeled here) is well-fitted into the GDGT density map. The color scheme is identical to that in Fig. 2*A*.

cytoplasm during capsid assembly because they are tightly integrated in the clefts formed by VP1, VP4, B210, and C131 (*SI Appendix*, Fig. S11). It was estimated that the mass ratio of lipids to proteins was 1:2.4 in SSV1 (29). We also observed that the spindle-shaped SSV19 particles became oval-shaped after treatment with chloroform (*SI Appendix*, Fig. S10*B*). Thus, whether additional lipids exist, possibly internally, in the SSV19 virion remains to be determined.

Ultrathin sections of the SSV19-infected cells show that SSV19 particles adsorb to the host cell membrane through the tail after penetrating the S-layer (*SI Appendix*, Fig. S12). We propose that the tailspikes bind specific glycan chains in the host receptor and disrupt the carbohydrate lawn associated with the S-layer, possibly by degrading the polysaccharides, in a fashion similar to the hydrolysis of O antigen of the lipopolysaccharide by the tailspike of P22 bacteriophage (32). The process of membrane penetration is probably facilitated by the GDGT lipids. Because the channel of the tail nozzle (Fig. 3*B*) is too narrow for the passage of the circular dsDNA genome, the tail may undergo drastic conformational changes to allow the delivery of the viral genome. Although the spindle-shaped morphotype is not found among bacterial or eukaryotic viruses, the similar tail structures and the mechanisms of genome delivery revealed in SSV19, herpesvirus, and bacteriophages suggest that these viruses originate from a common ancestor before the divergence of its host into the three domains of life.

Materials and Methods

Preparation of SSV19 Virions. SSV19 virions were prepared as described previously (8). Briefly, *Sulfolobus* sp. E11-6 infected with SSV19 was grown in liquid PSCVY medium for 5 d with shaking at 75 °C to an OD_{600} of ∼1.0. The culture was centrifuged at 5,000 × *g* for 20 min at 4 °C, and the supernatant was filtered through a 0.45-μm filter and centrifuged at 120,000 × *g* for 1 h at 4 °C. The pellet was resuspended in Zillig's basal salts, and the sample was subjected to two runs of cesium chloride density gradient centrifugation with a final CsCl concentration of 0.45 g/mL at 200,000 × *g* for 24 h at 4 °C. The purified virions were washed by ultrafiltration through a 30-kDa centrifugal filter unit (Merck Millipore).

Ultrathin Section of SSV19-Adsorbed Cells. *Sulfolobus* sp. E11-6 harboring SSV19 was grown to logarithmic phase (OD_{600} = 0.5), and the culture was centrifuged at 5,000 × *g* for 20 min. The cells were resuspended in Zillig's basal salts, and SSV19 virions were added to the cell suspension to a multiplicity of infection (MOI) of ∼10^4. Following incubation for 0.5 h at room temperature, the samples were frozen in the high pressure freezer (Leica HPM100, Germany). The fast-frozen samples were immersed into a freezing tube containing 1% osmium tetroxide in 100% acetone and placed in a freeze substitution device (Leica EM AFS, Germany) for 3 d at −90 °C, and then slowly warmed to −60 °C in 12 h, −30 °C in 12 h, and finally to 0 °C. Following freezing substitution, acetone was changed three times at a 15-min interval at 0 °C and once at room temperature. The samples were stained in 0.5% (wt/vol) uranyl acetate (UA) in acetone at 4 °C for overnight and then slowly infiltrated with SPI Pon 812 resin by placing them in mixtures of acetone and resin of different grades (25%, 50%, 75%, 100% vol/vol). The liquid resin was then polymerized at 60 °C for 48 h. Ultrathin sections were obtained by using an ultramicrotome (Leica EM UC6, Germany) equipped with a diamond knife and placed on a TEM grid, and stained with 2% (wt/vol) UA and observed under a JEM-1400 transmission electron microscope (JEOL).

Lipid Analysis. Samples of the exponentially-grown *Sulfolobus* sp. E11-6 cells and the purified SSV19 virions were lyophilized in a Speed-Vac concentrator, resuspended in chloroform/methanol (1:1), sonicated, and incubated at 65 °C for 16 h. After centrifugation, the supernatant was lyophilized and redissolved in petroleum ether/ethyl acetate (5:1). The samples were subjected to thin layer chromatography (TLC) on a Merck silica 60 plate in petroleum ether/ethyl acetate (5:1) for 2 h at 4 °C. After the run, the plate was developed with iodine overnight in a sealed chamber.

Negative-Stain EM. SSV19 virions and chloroform-treated SSV19 virions were stained with 2% (wt/vol) UA and observed under a JEM-1400 transmission electron microscope (JEOL), respectively.

Cryo-EM, Image Processing, and Structure Analysis. An aliquot (3.5 μL) of the SSV19 virion was applied to a glow-discharged Quantifoil holey carbon grid (R 2/2, 400 mesh) and plunged into liquid ethane using an FEI Vitrobot operated at 8 °C and 100% humidity. Frozen SSV19 virions were imaged at 78,000 × magnification, corresponding to a pixel size of 1.27 Å, with an exposure time of 1.275 s in a FEI Tecnai Artica 200 kv electron microscope. The electron dose of ∼35 e^-/A^2 was fractionated into 30 movie frames, which were aligned and averaged to a single image. The defocus value of each image was measured by GCTF in RELION (14). A total of 109,865 SSV19 particle images were boxed out from the 3,770 images. Two-dimensional (2D) and 3D-classifications were performed on the particle images using RELION. After multiple rounds of 2D- and 3D-classifications, four subsets of particle images were selected and subjected to auto-refinement. Finally, four capsid structures at 10.5, 10.0, 10.4, and 10.3 Å resolutions, respectively, were obtained. Based on the reconstructed capsid structures and the orientation and center of each particle image, the center of the virus tail in each particle image was calculated to box out the tail image from each particle image. The same reconstruction procedure was performed on all 49,361 tail images using RELION. The final resolution of the tail structure was 6.5 Å.

The orientation and center parameters of each tail image were further refined using a local refinement and reconstruction method. We used the tail structure segmented from the whole capsid structure as the model to refine the orientation and center of each tail image. The reconstruction and refinement were performed iteratively to improve the resolution until the orientations and centers of all tail images were stabilized and the tail structure could not be further improved. A soft-mask was used for the region of local refinement in each image.

Atomic Model Building and Refinement. The models of the capsid protein were built based on the cryo-EM density maps using the COOT software (33) and refined using real-space refinement as implemented in Phenix (34). Refinement and validation statistics are presented in *SI Appendix*, Table S1.

Data Availability. The atomic coordinates for the SSV19 tail have been deposited in the Protein Data Bank under accession code 7XDI (35). The density maps

for the tail and the SSV19 virion have been deposited in the EM Data Bank under accession codes EMD-33148 (36) and EMD-33149 (37), respectively. All study data are included in the article and/or *SI Appendix*, See also Movie S1.

ACKNOWLEDGMENTS. The cryo-EM experiment was carried out at Cryo-EM Platforms of Tsinghua University, Branch of the National Center for Protein Sciences. The thin section experiments were carried out at the Center for Biological Imaging (CBI), Institute of Biophysics, Chinese Academy of Sciences. We thank Li Wang from the Institute of Biophysics, Chinese Academy of Sciences, and Jiawei Wang from Tsinghua University for their assistance with EM sample preparation and atomic model building, respectively. This research was supported by the National Natural Science Foundation of China (12034006, 31970170, 91951000, 32071209, and 31971122) and the Natural Science Foundation of Hunan Province, China (2019JJ10002).

Author affiliations: [a]Key Laboratory for Matter Microstructure and Function of Hunan Province, Institute of Interdisciplinary Studies, Key Laboratory of Low-dimensional Quantum Structures and Quantum Control, School of Physics and Electronics, Hunan Normal University, Changsha, 410081 China; [b]State Key Laboratory of Microbial Resources, Institute of Microbiology, Chinese Academy of Sciences, Beijing, 100101 China; [c]College of Life Science, University of Chinese Academy of Sciences, Beijing, 100049 China; and [d]Technology Center for Protein Sciences, School of Life Sciences, Tsinghua University, Beijing, 100084 China

1. C. R. Woese, G. E. Fox, Phylogenetic structure of the prokaryotic domain: The primary kingdoms. *Proc. Natl. Acad. Sci. U.S.A.* **74**, 5088–5090 (1977).
2. C. R. Woese, O. Kandler, M. L. Wheelis, Towards a natural system of organisms: Proposal for the domains Archaea, Bacteria, and Eucarya. *Proc. Natl. Acad. Sci. U.S.A.* **87**, 4576–4579 (1990).
3. M. K. Pietilä, T. A. Demina, N. S. Atanasova, H. M. Oksanen, D. H. Bamford, Archaeal viruses and bacteriophages: Comparisons and contrasts. *Trends Microbiol.* **22**, 334–344 (2014).
4. H. Wang, N. Peng, S. A. Shah, L. Huang, Q. She, Archaeal extrachromosomal genetic elements. *Microbiol. Mol. Biol. Rev.* **79**, 117–152 (2015).
5. D. Prangishvili *et al.*, The enigmatic archaeal virosphere. *Nat. Rev. Microbiol.* **15**, 724–739 (2017).
6. M. Krupovic, E. R. J. Quemin, D. H. Bamford, P. Forterre, D. Prangishvili, Unification of the globally distributed spindle-shaped viruses of the Archaea. *J. Virol.* **88**, 2354–2358 (2014).
7. J. Wirth, M. Young, The intriguing world of archaeal viruses. *PLoS Pathog.* **16**, e1008574 (2020).
8. J. X. Zhang *et al.*, Novel *Sulfolobus* fuselloviruses with extensive genomic variations. *J. Virol.* **94**, e01624-19 (2020).
9. P. Contursi, S. Fusco, R. Cannio, Q. She, Molecular biology of fuselloviruses and their satellites. *Extremophiles* **18**, 473–489 (2014).
10. E. F. Rowland, M. A. Bautista, C. Zhang, R. J. Whitaker, Surface resistance to SSVs and SIRVs in pilin deletions of *Sulfolobus islandicus*. *Mol. Microbiol.* **113**, 718–727 (2020).
11. R. M. Ceballos, C. G. Drummond, C. L. Stacy, E. Padilla-Crespo, K. M. Stedman, Host-dependent differences in replication strategy of the *Sulfolobus* spindle-shaped virus strain SSV9 (a.k.a., SSVK1): Infection profiles in hosts of the family Sulfolobaceae. *Front. Microbiol.* **11**, 1218 (2020).
12. K. M. Stedman, M. DeYoung, M. Saha, M. B. Sherman, M. C. Morais, Structural insights into the architecture of the hyperthermophilic Fusellovirus SSV1. *Virology* **474**, 105–109 (2015).
13. C. Hong *et al.*, Lemon-shaped halo archaeal virus His1 with uniform tail but variable capsid structure. *Proc. Natl. Acad. Sci. U.S.A.* **112**, 2449–2454 (2015).
14. S. H. Scheres, RELION: Implementation of a Bayesian approach to cryo-EM structure determination. *J. Struct. Biol.* **180**, 519–530 (2012).
15. G. C. Lander *et al.*, The P22 tail machine at subnanometer resolution reveals the architecture of an infection conduit. *Structure* **17**, 789–799 (2009).
16. W. Chen *et al.*, Structural changes of a bacteriophage upon DNA packaging and maturation. *Protein Cell* **11**, 374–379 (2020).
17. A. S. Olia, P. E. Prevelige, Jr, J. E. Johnson, G. Cingolani, Three-dimensional structure of a viral genome-delivery portal vertex. *Nat. Struct. Mol. Biol.* **18**, 597–603 (2011).
18. A. Cuervo *et al.*, Structures of T7 bacteriophage portal and tail suggest a viral DNA retention and ejection mechanism. *Nat. Commun.* **10**, 3746 (2019).
19. A. A. Simpson *et al.*, Structure of the bacteriophage phi29 DNA packaging motor. *Nature* **408**, 745–750 (2000).
20. Y. T. Liu, J. Jih, X. Dai, G. Q. Bi, Z. H. Zhou, Cryo-EM structures of herpes simplex virus type 1 portal vertex and packaged genome. *Nature* **570**, 257–261 (2019).
21. C. Machón *et al.*, Atomic structure of the Epstein-Barr virus portal. *Nat. Commun.* **10**, 3891 (2019).
22. D. T. Jones, Protein secondary structure prediction based on position-specific scoring matrices. *J. Mol. Biol.* **292**, 195–202 (1999).
23. P. Redder *et al.*, Four newly isolated fuselloviruses from extreme geothermal environments reveal unusual morphologies and a possible interviral recombination mechanism. *Environ. Microbiol.* **11**, 2849–2862 (2009).
24. D. R. Jones *et al.*, Analysis of active site architecture and reaction product linkage chemistry reveals a conserved cleavage substrate for an endo-alpha-mannanase within diverse yeast mannans. *J. Mol. Biol.* **432**, 1083–1097 (2020).
25. M. van Wolferen *et al.*, Species-specific recognition of *Sulfolobales* mediated by UV-inducible pili and S-layer glycosylation patterns. *MBio* **11**, e03014-19 (2020).
26. R. Hartman *et al.*, The molecular mechanism of cellular attachment for an archaeal virus. *Structure* **27**, 1634–1646.e1633 (2019).
27. D. Ptchelkine *et al.*, Unique architecture of thermophilic archaeal virus APBV1 and its genome packaging. *Nat. Commun.* **8**, 1436 (2017).
28. R. Hochstein *et al.*, Structural studies of *Acidianus* tailed spindle virus reveal a structural paradigm used in the assembly of spindle-shaped viruses. *Proc. Natl. Acad. Sci. U.S.A.* **115**, 2120–2125 (2018).
29. E. R. J. Quemin *et al.*, *Sulfolobus* spindle-shaped virus 1 contains glycosylated capsid proteins, a cellular chromatin protein, and host-derived lipids. *J. Virol.* **89**, 11681–11691 (2015).
30. E. R. J. Quemin *et al.*, Eukaryotic-like virus budding in Archaea. *MBio* **7**, e01439-16 (2016).
31. S. M. Jensen, M. Brandl, A. H. Treusch, C. S. Ejsing, Structural characterization of ether lipids from the archaeon *Sulfolobus islandicus* by high-resolution shotgun lipidomics. *J. Mass Spectrom.* **50**, 476–487 (2015).
32. C. Wang, J. Tu, J. Liu, I. J. Molineux, Structural dynamics of bacteriophage P22 infection initiation revealed by cryo-electron tomography. *Nat. Microbiol.* **4**, 1049–1056 (2019).
33. P. Emsley, K. Cowtan, Coot: Model-building tools for molecular graphics. *Acta Crystallogr. D Biol. Crystallogr.* **60**, 2126–2132 (2004).
34. P. D. Adams *et al.*, PHENIX: A comprehensive Python-based system for macromolecular structure solution. *Acta Crystallogr. D Biol. Crystallogr.* **66**, 213–221 (2010).
35. Z. Han *et al.*, Structural insights into a spindle-shaped archaeal virus with a sevenfold symmetrical tail. Protein Data Bank. https://www.rcsb.org/structure/unreleased/7XDI. Deposited 27 March 2022.
36. Z. Han *et al.*, Structural insights into a spindle-shaped archaeal virus with a sevenfold symmetrical tail. EMDB:EMD-33148. https://www.ebi.ac.uk/emdb/. Deposited 27 March 2022.
37. Z. Han *et al.*, Structural insights into a spindle-shaped archaeal virus with a sevenfold symmetrical tail. EMDB:EMD-33149. https://www.ebi.ac.uk/emdb/. Deposited 27 March 2022.